The Astrophysical Journal, 961:25 (15pp), 2024 January 20 https://doi.org/10.3847/1538-4357/ad09e6

The Scaling of Vortical Electron Acceleration in Thin-current Magnetic Reconnection and Its Implications in Solar Flares

C. Crawford[1,2], H. Che[1,2], and A. O. Benz[3,4]
[1] Center for Space Plasma and Aeronomic Research (CSPAR), University of Alabama in Huntsville, Huntsville, AL 35805, USA
[2] Department of Space Science, University of Alabama in Huntsville, Huntsville, AL 35899, USA
[3] University of Applied Sciences and Arts Northwestern Switzerland, CH-5210 Windisch, Switzerland
[4] Institute for Particle Physics and Astrophysics, ETH Zürich, 8093, Zürich, Switzerland
Received 2022 December 30; revised 2023 September 25; accepted 2023 November 1; published 2024 January 11

Abstract

To investigate how magnetic reconnection (MR) accelerates electrons to a power-law energy spectrum in solar flares, we explore the scaling of a kinetic model proposed by Che & Zank (CZ) and compare it to observations. Focusing on thin current sheet MR particle-in-cell (PIC) simulations, we analyze the impact of domain size on the evolution of the electron Kelvin–Helmholtz instability (EKHI). We find that the duration of the growth stage of the EKHI ($t_G \sim \Omega_e^{-1}$) is short and remains nearly unchanged because the electron gyrofrequency Ω_e is independent of domain size. The quasi-steady stage of the EKHI ($t_{\rm MR}$) dominates the electron acceleration process and scales linearly with the size of the simulations as $L/v_{\rm A0}$, where $v_{\rm A0}$ is the Alfvén speed. We use the analytical results obtained by CZ to calculate the continuous temporal evolution of the electron energy spectra from PIC simulations and linearly scale them to solar flare observational scales. For the first time, an electron acceleration model predicts the sharp two-stage transition observed in typical soft–hard–harder electron energy spectra, implying that the electron acceleration model must be efficient with an acceleration timescale that is a small fraction of the duration of solar flares. Our results suggest that we can use PIC MR simulations to investigate the observational electron energy spectral evolution of solar flares if the ratio $t_{\rm MR}/t_G$ is sufficiently small, i.e., $\lesssim$10%.

Unified Astronomy Thesaurus concepts: Solar energetic particles (1491); Solar magnetic reconnection (1504); Solar flares (1496)

1. Introduction

Magnetic reconnection (MR) is an essential mechanism in the interpretation of solar flares (Lin 2011; Benz 2017), and it is thought to release the magnetic energy stored in solar flare magnetic loops through the topological change of the magnetic field. During solar flares, more than 50% of the magnetic energy is converted into the kinetic energy of the particles (Lin 2011; Vilmer 2012). A ubiquitously observed feature of the energetic particles is the inverse power-law energy spectrum. However, the way MR accelerates particles in solar flares remains an open question.

Electron acceleration in solar flares has been observed extensively due to its rich and intense radiation from radio to gamma-ray. Some common features associated with the solar energetic electrons have been found (see Section 2.2). Spectral observations of the hard X-ray (HXR) $E > 10$ keV emission from solar flares have shown the following: (1) solar flares commonly produce an inverse power-law energy spectrum $f(W) \propto W^{-\alpha}$ (where W is the electron kinetic energy, and α is the spectral index) (Lin 2011; Benz 2017); (2) solar flares can accelerate a huge number of electrons ($\sim 10^{35}$) on very short timescales (less than 1 s or $\sim 10\Omega_i^{-1}$ in the corona, where Ω_i is the ion gyrofrequency), which are restricted by the energy loss caused by collisions (Benz 2017); (3) the HXR spectral indices can exhibit either soft–hard–soft (SHS) or soft–hard–harder (SHH) evolution in single peaks and in the overall evolution. These behaviors are characterized by an initially soft spectrum that hardens during increasing emission, and then it either softens again (SHS) or continues to harden (SHH) after the emission peaks.

Particle acceleration is a fully kinetic process, and it requires a fully kinetic treatment. Extensive studies have been performed on modeling the generation of the inverse electron energy power-law distribution. Some of the kinetic mechanisms, such as multi-island contraction acceleration in MR (Drake et al. 2006; Zank et al. 2014), are not efficient enough to produce power-law energy spectra in the desired timescale due to their adiabatic invariant acceleration property (Che & Zank 2019). Stochastic kinetic turbulence models can efficiently produce the desired spectra, but it is unclear how to produce the proposed kinetic turbulence in MR, and the kinetic turbulence is usually assumed to be fully developed (Pritchett & Wu 1979; Kliem 1994; Miller et al. 1997; Drake et al. 2006; Medvedev & Zakutnyaya 2009; Petrosian 2012; Nishizuka & Shibata 2013; Klein & Dalla 2017).

Recently, a promising model was introduced by Che & Zank (2020; hereafter referred to as the CZ model or CZ). In this vortical MR model, an electron Kelvin–Helmholtz instability (EKHI) is triggered during particle-in-cell (PIC) MR simulations with force-free currents in low-β plasmas ($\beta = 8\pi n k_B T/B^2 \ll 1$), a common type of guide field MR in solar flares. The EKHI creates expanding magnetic vortices inducing stochastic electric fields inside the vortices. The structures of the inductive electric field trap and accelerate electrons via a second-order Fermi acceleration process. CZ showed that the EKHI efficiently produces an inverse electron energy power-law distribution of the form $f(W) \propto W^{-\alpha}$ within a few ion gyroperiods (see Section 2.1). This model produces a two-stage SHH evolution with an index similar to observations of solar energetic electrons, and the acceleration timescale is also well

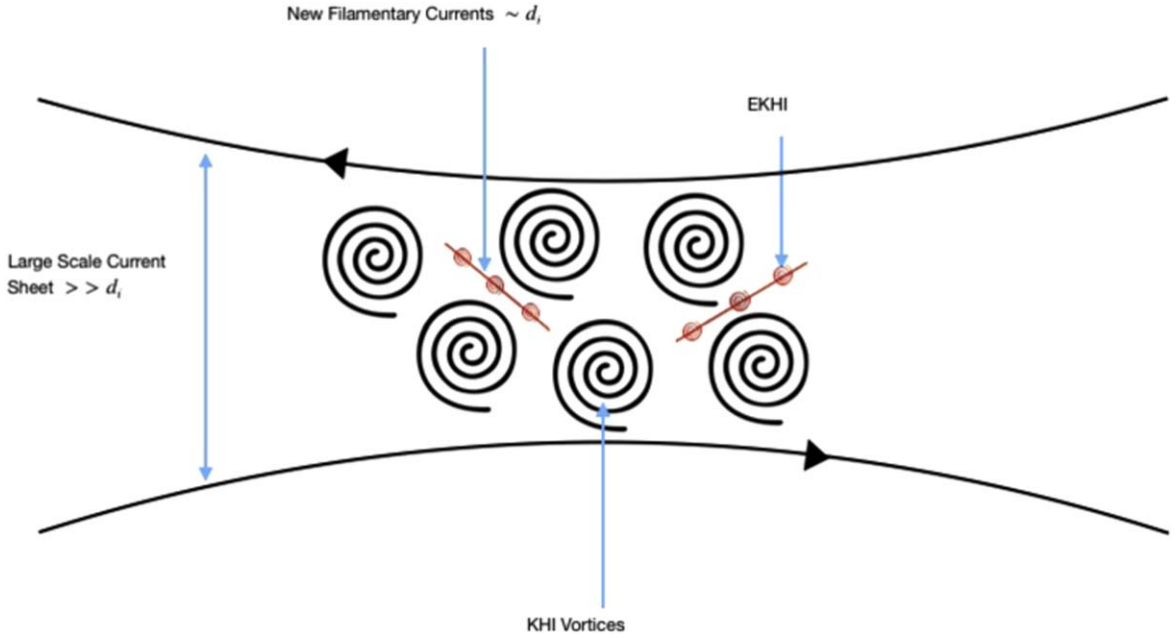

Figure 1. A schematic diagram of large-scale ($\gg d_i$) current sheets with KHI vortices. Due to the turbulence, small-scale ($\sim d_e$) filamentary currents form and lead to EKHI development.

within the expected electron acceleration timescale in solar flares. While this model remains promising, the PIC simulation domain is too small in comparison with solar flares (MHD scale) due to the current computational capabilities. PIC simulations on an MHD scale require too much time and computational power to be feasible. Moreover, how to model the features found in PIC simulations (the power-law energy spectrum and the two-stage evolution) in a uniform manner and compare them with observations remains a challenging question.

The initial width of the current sheet in MHD MR is much larger than the ion inertial length $d_i = c/\omega_{pi}$, where ω_{pi} is the ion plasma frequency, c is the speed of light, and d_i is the typical width of the current sheet in PIC simulations. The condition for MR to occur is that the current sheet must thin to the electron inertial length $\sim d_e = c/\omega_{pe}$, where ω_{pe} is the electron plasma frequency, for the electron frozen-in condition $\boldsymbol{E} + \boldsymbol{v_e} \times \boldsymbol{B}/c = 0$ to be broken. Magnetospheric Multiscale Mission (MMS) observations confirm this theoretical expectation (Burch et al. 2016; Kuramitsu et al. 2018; Torbert et al. 2018). In such a case, MHD MR has two possible evolutions. One possibility is where the current sheet keeps thinning to the electron kinetic scale, but this is unlikely to occur since it is common that instabilities are triggered with the proceeding of MR. For example, it is common that the tearing instability is driven by the magnetic shear stored in the current sheet. However, recent studies show that with the thinning of the Harris current sheet, the velocity shear carried by ions is accumulated and becomes stronger, eventually triggering MHD Kelvin–Helmholtz instability (KHI) and quickly suppressing the tearing instability due to the faster growth rate of KHI (Karimabadi et al. 2013; Kowal et al. 2020; Borgogno et al. 2022). The primary difference between KHI and tearing instability is that KHI generates magnetic vortices (magnetic turbulence), while tearing instability generates plasmoids that act similarly to magnetic islands in MR (Drake et al. 2006). KHI generates vortices, and the merging of vortices triggers kinetic-scale MR (Karimabadi et al. 2013; Kowal et al. 2020; Borgogno et al. 2022; see Figure 1). We focus on force-free MR, in which velocity shear becomes stronger because $\boldsymbol{j} \times \boldsymbol{B} = 0$. On the MHD scale, ions dominantly carry the momentum; thus, v_i is proportional to the antiparallel reconnection magnetic field. Based on this picture, we propose a KHI turbulent force-free MR acceleration model in which small-scale MRs are triggered in thin current sheets of $\sim d_i$ caused by MHD-scale KHI. The model is similar to some other MHD-scale turbulent reconnection models, e.g., the stochastic MR model by Lazarian & Vishniac (1999), which is supported by some evidence in observations of solar flares (Raymond et al. 2012). On the kinetic scale, compared to the kinetic tearing instability, the EKHI growth rate is about the electron gyrofrequency Ω_e, which is much faster than the kinetic tearing instability, whose growth rate is smaller than Ω_i (Daughton et al. 2011). Thus, in low-β plasma, if triggered, similar to large-scale KHI, EKHI can always suppress tearing instability.

In this paper, instead of directly performing MHD-scale PIC simulations to study the large-scale electron acceleration in MR, we use an alternative method in which we investigate the scaling of the EKHI acceleration in thin current sheet MR and its implications in solar flares. Using PIC simulations of MR with different domain sizes, we focus on how ion-scale current sheets thin to an electron scale and trigger EKHI that accelerates electrons. Thin current sheet ($\sim d_i$) MR allows us to study how simulation domain size affects the nonlinear EKHI evolution with affordable computational costs (see Section 5). This helps us to understand how to scale and apply our PIC simulation results to MHD-scale models that can be directly compared with observations, such as the observations of solar flares. At the end of the paper, we present the conclusion and a discussion (see Section 6).

2. Introduction to the Vortical Reconnection Acceleration Model and Solar Flare Observations of Electron Acceleration

2.1. Vortical Reconnection Acceleration Model

Force-free magnetic fields are common in the solar corona, and the associated force-free current sheets are particularly interesting in solar flares, whose magnetic energy is released

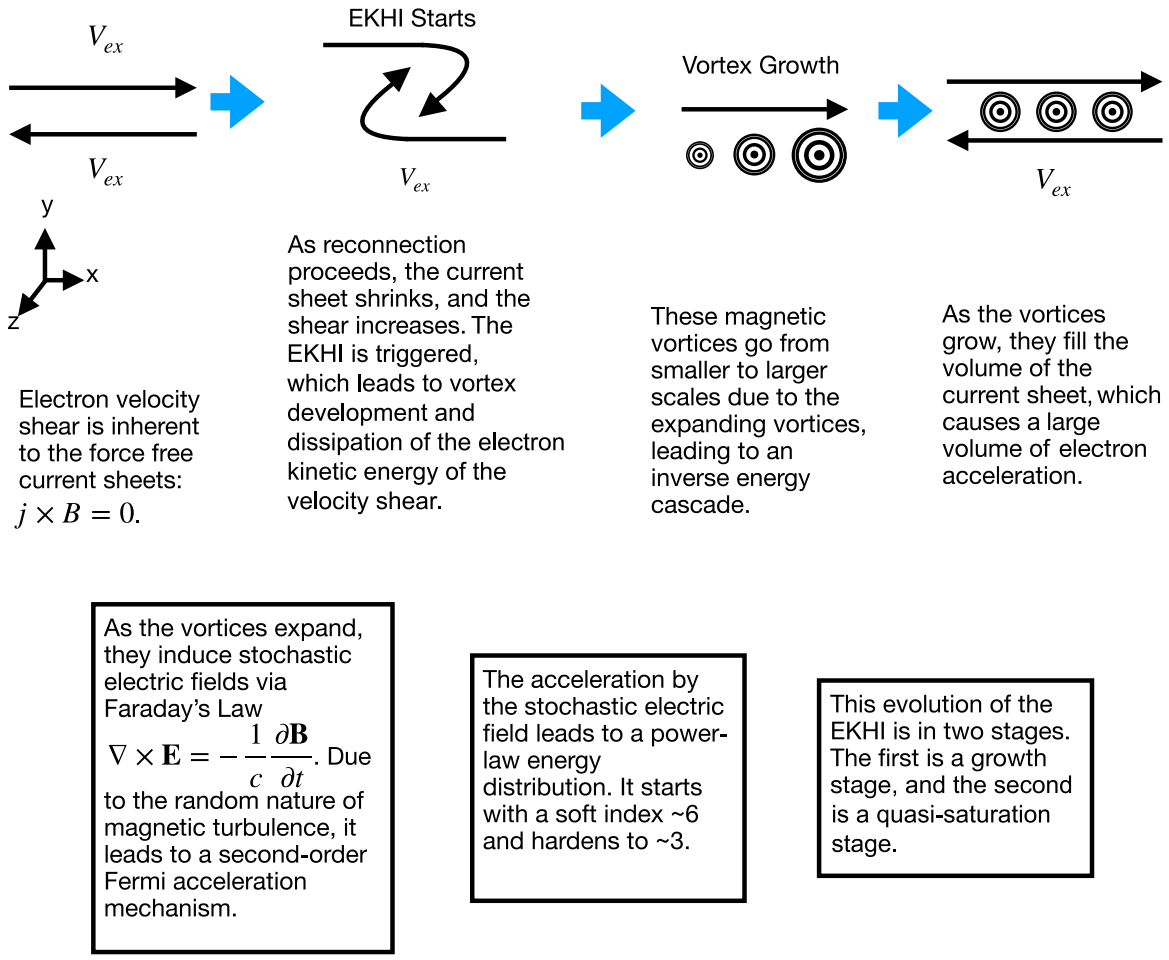

Figure 2. A schematic diagram of the EKHI acceleration mechanism.

through MR. The force-free condition is $\boldsymbol{j} \times \boldsymbol{B} = 0$, where $\boldsymbol{j}$ is parallel to $\boldsymbol{B}$. Electrons are the main carriers in current sheets on kinetic scales due to their small mass, so we can approximate $\boldsymbol{j}$ as $\boldsymbol{j_e}$. Let us assume that the reconnection plane is in the x–y plane and initially $\boldsymbol{j_{ez}}(y) = j_{ex}\hat{x} + j_{ez}\hat{z}$ (see Figure 2). With the coordinates we use, the magnetic field associated with $\boldsymbol{j_{ez}}$ can be written as $\boldsymbol{B} = B_x\hat{x} + B_z\hat{z}$. Using Ampere's law with force-free currents, $\boldsymbol{j_e} \times \boldsymbol{B} = \nabla \times \boldsymbol{B} \times \boldsymbol{B}$. It is easy to show that the force-free condition leads to $B_x^2 + B_z^2 = C^2$, where C is a constant. $\boldsymbol{j_e} \times \boldsymbol{B} = 0$ gives the following equation:

$$v_{ex} = v_{ez} B_x / B_z, \tag{1}$$

showing that the electron velocity v_{ex} follows the antiparallel MR field B_x and thus causes the electron velocity shear to be inherent in force-free current sheets.

Because of the inherent electron velocity shear, the development of an EKHI is a natural step in the evolution of MR with a force-free current sheet. As MR proceeds in a force-free current sheet, the current sheet shrinks to the electron inertial scale d_e and forms x-line geometry, while the antiparallel velocity shear simultaneously increases and triggers an EKHI whose growth rate is about Ω_e. The EKHI begins by developing small-scale velocity and magnetic vortices (see Figure 2) that dissipate the electron kinetic energy associated with the velocity shear v_{ex} and transfer it to magnetic energy. As the vortices continue to evolve, they grow from the electron kinetic scale ($\sim d_e$) to ion kinetic scales ($\sim d_i$) leading to an inverse energy cascade.

As the vortices grow in the x–y plane, they fill the current sheet, while the electrons are continually accelerated. Assuming the conservation of the 2D magnetic flux holds, $B_{x0}R_0 \sim B_{xt}R_t$ where the mean antiparallel magnetic field B_{xt} and R_t the radius of the 2D vortex represent these quantities at a time t after the start of the growth. As the radius of the vortices R_t increases, the magnitude of the mean magnetic field decreases, which leads to an induced electric field via Faraday's law:

$$\nabla \times \boldsymbol{E} = -\frac{1}{c}\frac{\partial \boldsymbol{B}}{\partial t}. \tag{2}$$

The induced electric field is stochastic due to the self-similar nature of the magnetic turbulence whose power spectrum demonstrates a power law. As a result, the electric field accelerates electrons stochastically, which is shown to be a second-order Fermi acceleration, $\delta v_{ez}/\delta t \sim \frac{1}{2}(v_L/c)^2 v_{ez}/\tau_g$, where $(v_L/c)^2 \ll 1$, v_L is the electron gyrovelocity, and τ_g is the growth time of the EKHI (Che & Zank 2020). The second-order Fermi acceleration mechanism leads to an electron power-law energy distribution,

$$f(W) \propto W^{-(1+4a^2D/R)/2}, \tag{3}$$

where $a = B_{\rm null}/B_0$; $B_{\rm null}$ is the magnetic field at the null point, which is defined as $B_{\rm null} = B_g + 1$; B_0 is the asymptotic magnetic field; B_g is the magnetic guide field; and D and R are the spatial scales of the inductive electric field and magnetic vortices, respectively (Che & Zank 2020).

The EKHI experiences a two-stage evolution: a growth stage followed by a quasi-steady stage of turbulence. The magnetic turbulence spectra of the vortices show a hard-to-soft two-stage evolution correlated with the growth and quasi-steady stages of the EKHI. Due to the acceleration caused by the induced electric field, the electron power-law energy distribution demonstrates a similar SHH two-stage evolution with an index evolution from ∼6 to ∼3.

Compared to the multi-island acceleration model (Drake et al. 2006), EKHI accelerates electrons through the expansion of magnetic vortices. Magnetic vortices are a type of magnetic turbulence that induces stochastic electric fields while expanding. Multi-islands are produced by tearing instability and accelerate electrons through adiabatic motions to absorb the magnetic energy released by the contraction of the islands. Therefore, the multi-island acceleration timescale is comparable to the MHD MR process, and it is difficult to obtain the fully kinetic electron power-law energy spectra within the desired timescale due to the particle confinement of magnetic islands (Che & Zank 2019). As a comparison, the magnetic vortical MR acceleration process (a stochastic process) can produce the desired power-law energy spectra within about the ion gyrofrequency Ω_i, which is a tiny fraction of the whole MR process (Che & Zank 2020; Che et al. 2021).

2.2. A Brief Introduction to Solar Energetic Electrons

Observations have discovered that solar flares accelerate electrons on very short timescales and develop a power-law energy distribution with a two-stage evolution. The theory requires the timescale for solar flare electron acceleration to be shorter than the collisional energy-loss timescale, which puts an upper limit on the electron acceleration timescale (Benz 2017):

$$\tau_{\rm coll}(E_{\rm kin}) = 0.31\left(\frac{v}{10^{10}\ {\rm cm\ s^{-1}}}\right)^3\left(\frac{10^{11}\ {\rm cm^{-3}}}{n_e}\right). \quad (4)$$

In the solar corona, $n_e \sim 10^8$–$10^{11}\ {\rm cm^{-3}}$, and $v \sim 0.1c$–$0.5c$, which are typical for energetic electrons. This gives a range of $\tau_{\rm coll} \sim 8 \times 10^{-1}$ to 10^{-3} s, meaning that for a typical flare whose duration is ∼1000 s, the electron acceleration is very efficient, and it is only about 1/1000 of a flare's timescale. Comparing this to the EKHI acceleration, the timescale is $\sim\Omega_i^{-1}$ using $B \sim 1$ G, giving $\Omega_i^{-1} \sim 10^{-4}$ s, which is sufficiently small for electron acceleration to occur and is extremely efficient. This condition can rule out the multi-island acceleration model because of its much longer acceleration timescale.

Solar flare electron energy spectra are inferred from X-ray flux spectra and often described using a power law in energy $F(E) = AE^{-\lambda}$. The relationship between the X-ray flux spectra observed from the solar corona and the electron energy power law can be predicted using a simple result, $\alpha \sim \lambda + 1$ (Brown 1971; Aschwanden 2002), where α is the electron energy spectrum index, and λ is the X-ray photon index. The spectral observations in the HXR emission of solar flares can exhibit what is referred to as SHS or SHH evolution. SHS evolution is characterized by an initially soft spectral power-law index that becomes hard during increasing emission and then soft again after the emission peaks. SHH is characterized by an initially soft spectral power-law index that becomes hard during increasing emission and then harder still after the emission peaks (Kepa et al. 2020). EKHI vortex acceleration demonstrates an evolution similar to observational SHH spectra. For this reason, in this paper, we focus on comparing our simulation to SHH observations and will have a discussion about the SHS evolution in Section 6.

Table 1
Spatial Scale of the Simulations

	1 L64W32	2 L128W32	3 L128W64
L	$64d_i$	$128d_i$	$128d_i$
W	$32d_i$	$32d_i$	$64d_i$

Note. Each simulation as described by its domain size, with L being the length of the domain in the x-direction, and W being the width in the y-direction.

3. Simulation Setup

Based on the KHI turbulent MR acceleration model shown in Figure 1 (see Section 1), ion kinetic scale ($\sim d_i$) MR can well demonstrate the thinning of the current sheet to the electron kinetic scale ($\sim d_e$) and trigger EKHI. This paper will focus on MR with a thin force-free current sheet ($\sim d_i$) and investigate how the domain size impacts the development of the EKHI and electron acceleration.

In this paper, 2.5D PIC MR simulations are carried out using the p3d code (Zeiler et al. 2002) starting with double force-free current sheets, periodic boundary conditions, and a guide field. Following the 3D and 2.5D PIC simulations carried out by CZ, which found that the out-of-plane dimension only slightly impacts the acceleration results, we conducted three 2.5D PIC simulations with similar characteristics except for the use of three different domain sizes to study the evolution of the acceleration process: $L_x \times L_y = 128d_i \times 64d_i$, $L_x \times L_y = 128d_i \times 32d_i$, and $L_x \times L_y = 64d_i \times 32d_i$ with corresponding grid numbers $n_x \times n_y = 16384 \times 8192$, $n_x \times n_y = 16384 \times 4096$, and $n_x \times n_y = 8192 \times 4096$, which will be referred to as simulations L128W64, L128W32, and L64W32, respectively. The simulations are named according to Table 1, with L_x as L and L_y as W. We chose this closed sample of domain sizes to emphasize the effects of increasing the domain size in either L, W, or both. In Section 5, we show that the three domain sizes are sufficient to draw a basic picture of the electron acceleration by the EKHI and its scaling. Each simulation has a particle number per cell of 100 for each species. The guide field B_g is defined asymptotically, $B_x \to B_0$, as $y \to \infty$, which means that $B_g^2/B_0^2 = C^2 - 1$ (where C is a constant). It is selected so that the total magnetic field B is constant, $B^2 = B_x^2 + B_z^2 = 7.25B_0^2$, and the reconnection magnetic field, B_x, is initialized as $B_x/B_0 = \tanh[(y - W/2)/w_0]$, where B_0 is the asymptotic amplitude of B_x, and w_0 is the half-width of the initial current sheet, $w_0 = 0.5d_i$, where $d_i = c/\omega_{pi}$, $\omega_{pi} = (4\pi n_0 e^2/m_i)^{1/2}$ ω_{pi} is the initial ion plasma frequency. We initiate the reconnection magnetic field with out-of-plane double current sheets that have flipped directions. The double force-free current sheets guarantee that the periodic boundary condition is satisfied in both the x- and y-directions.

In these simulations, the initial densities of both ions and electrons are uniform, and $n_e = n_i = n_0$. The guide field B_g is

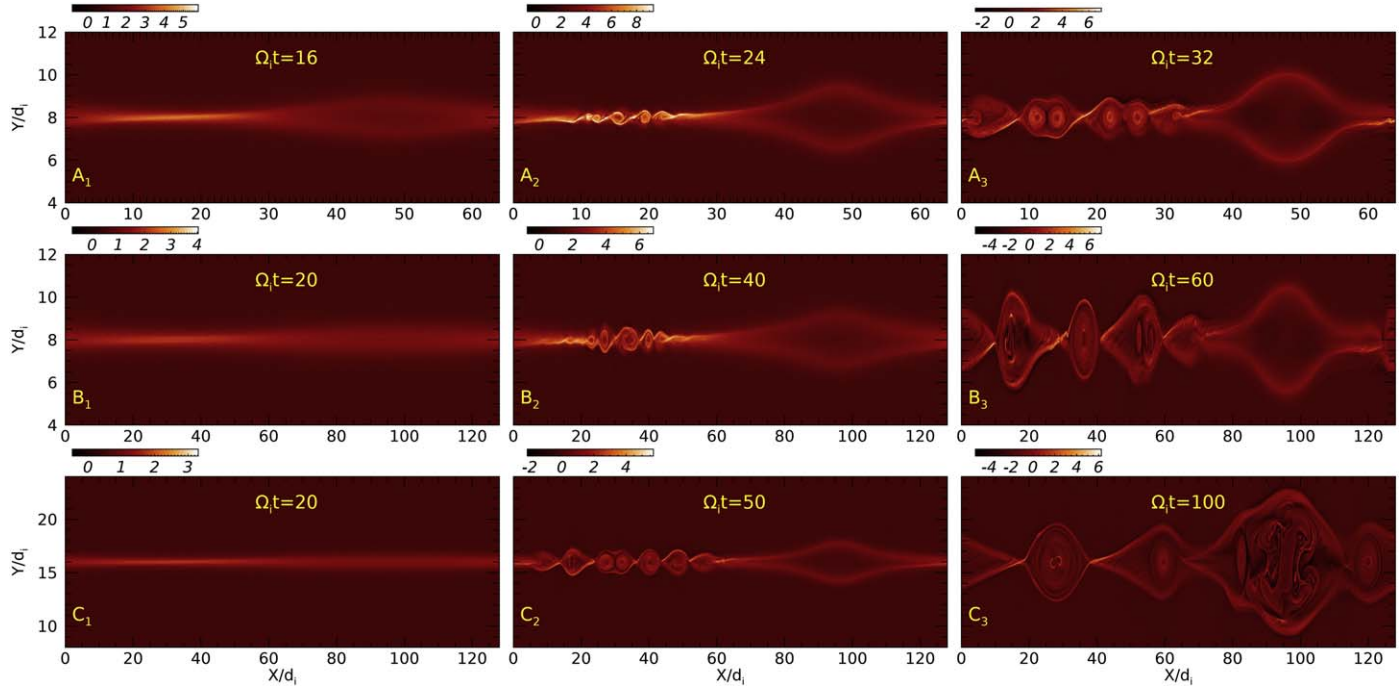

Figure 3. The evolution of j_{ez} obtained from the top current sheet for each simulation at different times (the initial double current sheets with flipped directions demonstrate a similar evolution). The x-line is initialized on the left half, while the magnetic island is on the right half. The top panels demonstrate the smallest simulation, L64W32 (A_1 through A_3); the middle panels demonstrate L128W32 (B_1 through B_3); and the bottom panels show L128W64 (C_1 through C_3). The vortices on the left side become visible in A_2, B_2, and C_2, and the islands are distinguishable via the near-zero j_{ez} in the center of A_2, B_2, and C_2. The color bars show the range of j_{ez}.

$B_g = 2.5B_0$. The ratio of the initial electron plasma frequency $\omega_{pe} = (4\pi n_0 e^2/m_e)^{1/2}$, the initial electron gyrofrequency Ω_e is $\omega_{pe}/\Omega_e = 2$, and the mass ratio is chosen to be $m_i/m_e = 100$. The initial velocity distribution functions for electrons and ions are isotropic Maxwellian distributions with temperatures $T_{e0} = T_{i0}$ and $\beta = 0.04$. In the simulation, the spatial distance is normalized to the initial d_i, and the temperature is normalized to $m_i v_{A0}^2$, where $v_{A0} = B_0/(4\pi n_0 m_i)^{1/2}$ is the asymptotic ion Alfvén wave speed, and the magnetic field is normalized to B_0, mass to m_i, velocity to v_{A0}, density to initial density n_0, and electric field to $E_0 = v_{A0}B_o/c$. For the top half of each simulation, MR is initialized to produce a primary x-line at $x = L_x/4$ and an island at $x = 3L_x/4$, while the bottom half of the simulation has the primary x-line at $x = 3L_x/4$ and the island at $x = L_x/4$. The simulation time for each domain is as follows: L128W64 has a simulation time of $\Omega_i t = 120$, L128W32 a time of $\Omega_i t = 60$, and L64W32 a time of $\Omega_i t = 40$, where $\Omega_i = eB_0/m_i c$ is the asymptotic ion gyrofrequency. The total simulation times are restricted to be shorter than L/v_{A0} to avoid the possible periodic boundary effects. Using the standard technique in PIC simulations, an initial small perturbation is introduced so that the MR can occur in a reasonable simulation timescale, much shorter than the timescale to develop current-driven instabilities.

4. Simulation Results

4.1. The Topology Change of MR and the Development of Magnetic Vortices

The three simulations with increasingly larger domain sizes are used to demonstrate the effect of the system's spatial scale on the evolution of EKHI and the corresponding electron acceleration. The initial double current sheets demonstrate similar physical processes; thus, in this paper, we select the top current sheet to demonstrate the simulation results. In Figure 3, we show the evolution of the magnetic vortices and islands during MR using the electron current density j_{ez} at different times. We use j_{ez} because of its relationship with the in-plane magnetic field $\boldsymbol{B}_{\rm ip} = B_x\hat{\boldsymbol{x}} + B_y\hat{\boldsymbol{y}}$ described by Ampere's law, $\nabla \times \boldsymbol{B}_{\rm ip} = j_{ez}\hat{\boldsymbol{z}}$. We notice that as the spatial scale of the simulation increases, MR requires more time to start and saturate, causing a delay in the growth of the magnetic island.

As MR proceeds, the initial perturbations develop an x-line on the left half of each simulation at $x/d_i = L/4$ and a magnetic island on the right half of each simulation at $x/d_i = 3L/4$. In the first column of Figure 3, A_1 at $\Omega_i t = 16$, B_1 at $\Omega_i t = 20$, and C_1 at $\Omega_i t = 20$, we can see that the early stages of the x-line and magnetic island form as the EKHI begins to be triggered where the velocity shear is the largest. During this early stage of EKHI, electron acceleration has already started, but the EKHI vortices are too small to see. Shortly after the early stage, the magnetic island continues to contract from an elongated shape to a rounder one releasing magnetic energy. We begin to see that the vortices develop on the left side of the current sheet (at $L_x/4$), as shown in the middle column of Figure 3 (A_2 at $\Omega_i t = 24$, B_2 at $\Omega_i t = 40$, and C_2 at $\Omega_i t = 50$). The difference between the vortices and magnetic islands is that the current density j_{ez} is near zero around the center of the islands, while it is fairly strong around the center of the vortices. The size of the vortices quickly increases from the initial electron inertial scale d_e to ion inertial scales d_i. As the simulation scale increases, more vortices develop, and then they begin interacting with one another while interacting weakly with the ends of the magnetic island. The ends of the island are at $x/d_i = 32$ and 64 for the smallest simulation and $x/d_i = 64$ and 128 for the larger two simulations. We note that the magnetic island in each

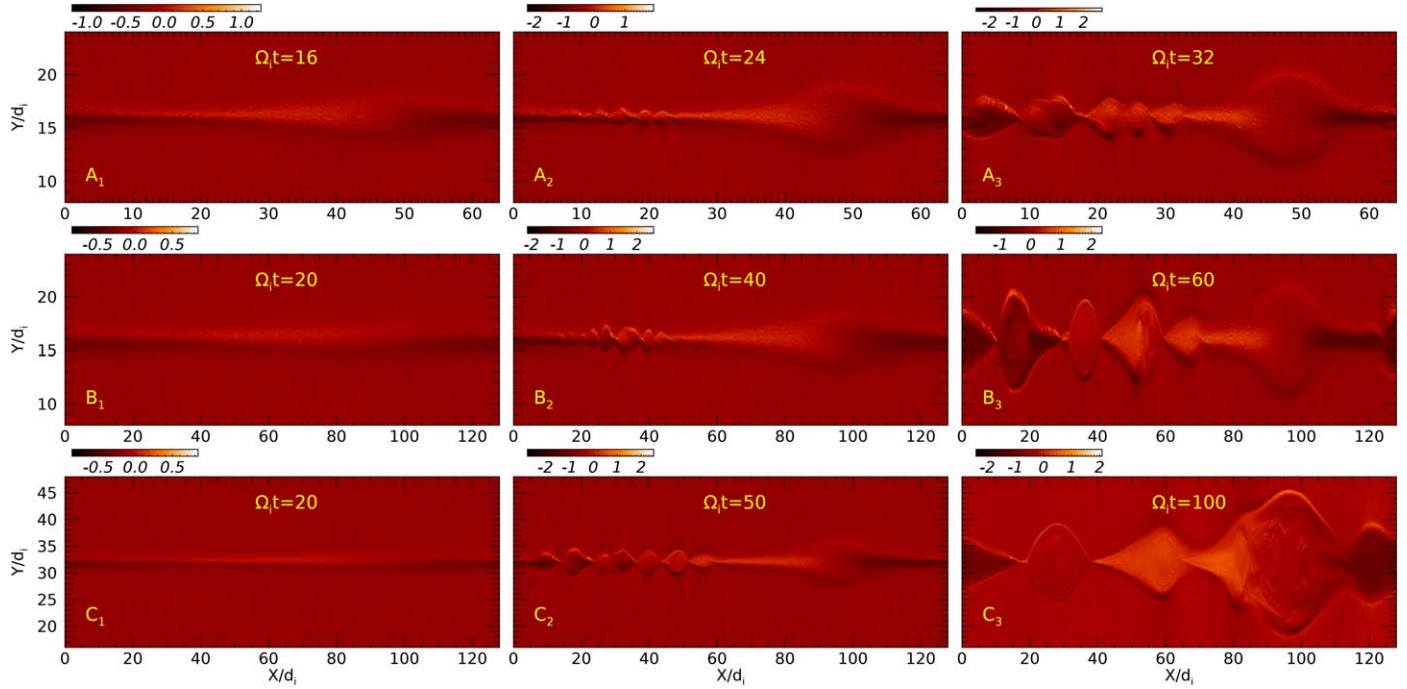

Figure 4. The evolution of V_{ex} for each simulation at different times, which shows the evolution of the velocity shear in the top half of the simulation domain. The top panels demonstrate the smallest simulation, L64W32 (A_1 through A_3); the middle panels demonstrate L128W32 (B_1 through B_3); and the bottom panels show L128W64 (C_1 through C_3). The color bars show the magnitude of the velocity shear $\boldsymbol{v_{ex}}$. The velocity shear is near zero around the center of the magnetic island.

simulation has very little effect on the triggering of the magnetic vortices.

As the vortices continue to evolve, they keep growing, and some of them eventually merge, causing more violent turbulence. We notice that in the smaller domain simulation (top row of Figure 3), the vortices begin to merge late in the simulation. The larger the domain size becomes, the earlier this merging begins. This is shown more clearly in Figure 3 B_2, which is slightly over halfway through the simulation, and C_2, which is less than halfway through. At a later time in the simulations, the vortices begin to interact with the magnetic island. In particular, for the largest simulation shown in Figure 3 C_3, some of the vortices become injected into the magnetic island and violently interact with it, deforming the island while generating turbulence. The spatial scale of the vortices increases nearly linearly with increases in the width of each simulation. Overall, the development of the magnetic islands does not significantly impact the EKHI and the formation of the vortices.

4.2. The Electron Velocity Shear and the Triggering of EKHI

In a similar fashion to the evolution of the magnetic vortices and magnetic island, we show the evolution of the electron fluid vortices generated by the inherent electron velocity shear caused by antiparallel $\boldsymbol{v_{ex}}$ in Figure 4. The antiparallel electron velocity following the antiparallel magnetic fields $v_{ex} = v_{ez}B_x/B_z$ (see Section 2.1) generates velocity shear at the center of the current sheet. During MR, the current sheet shrinks, and the velocity shear accumulates. The magnetic field along the electron velocity v_{ex} produces the magnetic tension that stabilizes the EKHI. Once the current sheet shrinks to the electron inertial scale d_e, the ideal frozen-in condition breaks down ($\boldsymbol{E} + \boldsymbol{v_e} \times \boldsymbol{B}/c \neq 0$). When the velocity shear is larger than the localized electron Alfvén wave velocity ($v_{Aex} = B_x/(4\pi n_e m_e)^{1/2}$) propagating along the reconnection magnetic field, i.e., when $|v_{ex}| > |v_{Aex}|$, the EKHI is triggered where the threshold $\Delta v_{ex} > 2V_{Ae}$ (Che & Zank 2023) is reduced to $|v_{ex}| > |v_{Aex}|$ because v_{ex} is nearly symmetric above and below the centerline.

To demonstrate the velocity shear threshold of the EKHI, we show images of the velocity shear of the smallest simulation (L64W32; $|v_{ex}| - |v_{Aex}|$) at the location very close to the center of the current sheet at three different times in Figure 5. The velocity shear does not distribute uniformly, and the mean is close to v_{Aex} (in many locations, $|v_{ex}| \ll |v_{Aex}|$, we have set the negative values to zero for visual clarity in Figure 5). As shown in this figure, the shear peaks near the center of the current sheet, and as time progresses, the velocity shear moves outward with the magnetic vortices as the magnetic field is also enhanced at the edge. Thus, the new EKHI is still triggered near the center of the current sheet because of the very small threshold v_{Aex} due to very small B_x. As a result, new magnetic vortices are continuously generated from the center of the current sheets, as we see in Figures 3 and 4, and the stochastic electric field is also continuously generated, which keeps the electron acceleration going.

As a comparison, the magnetic island shows a nearly zero velocity shear near its center and a much weaker δv_{ex} at the edge than that of the vortices, while the magnetic shear of the island is strong at the edge. As a result, the EKHI is difficult to excite in the island. At a later time, (A_3, B_3, and C_3) electron jets are produced from the vortices and penetrate into the island. In the largest simulation, the jets generate new vortices that violently merge with the island. However, we do not see that the physical process related to the magnetic island significantly impacts the generation of the EKHI or the generation and merging of the vortices. Thus, in the following, we will focus on the magnetic vortices and will not discuss the magnetic islands.

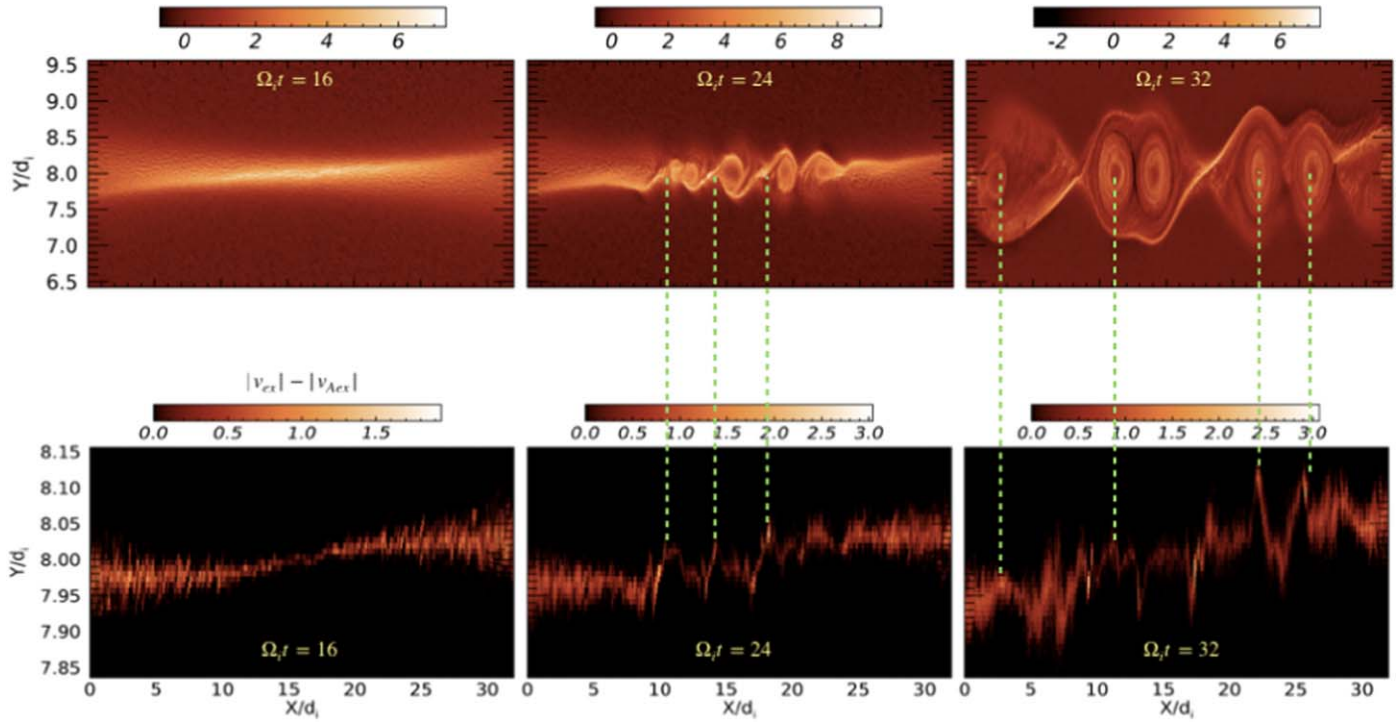

Figure 5. Zoomed-in images of the velocity shear ($|v_{ex}| - |v_{Aex}|$) compared to images of J_{ez} (the vortices) in the top left quarter of the simulation domain of the smallest simulation (L64W32) at three different times. The dotted green lines show the association of the peaks in the shear with the vortices. Negative values (of the velocity shear) are changed to zero in this figure for visual clarity.

4.3. Nonlinear Evolution of EKHI

With the growth of the magnetic vortices, the corresponding magnetic turbulence demonstrates a two-stage evolution: a growth stage followed by a quasi-steady stage. The growth stage includes a linear and nonlinear stage and overall is very short due to the fast growth rate of the EKHI ($\sim\Omega_e$). The growth stage is followed by the nonlinear quasi-steady stage, where the power-law magnetic energy spectra become steady, implying that the kinetic turbulence is fully developed. This stage is long and dominates the simulations.

The turbulent magnetic energy in each simulation develops a power-law spectrum around $\Omega_i t \sim 20$, which is at an early stage of the EKHI. It is represented by the green lines in Figure 6, where $\delta B^2 \propto k^{-2.1}$ for simulation L64W32, $\delta B^2 \propto k^{-2.0}$ for simulation L128W32, and $\delta B^2 \propto k^{-2.3}$ for simulation L128W64. During the continuous nonlinear evolution of the EKHI, the vortices expand, leading to continuous inverse energy cascades and merging of the magnetic vortices generating multiple x-points. More magnetic turbulence energy is transferred into longer wavelengths as time progresses. This is marked by the arrows from the green to red lines in Figure 6. When the EKHI nearly saturates, the power law becomes softer and stable: $\delta B^2 \propto k^{-3.0}$ for simulation L64W32, $\delta B^2 \propto k^{-2.9}$ for simulation L128W32, and $\delta B^2 \propto k^{-3.1}$ for simulation L128W64. This takes longer in the two larger simulations because of the increased magnetic energy available in MR. In Kolmogorov turbulence, energy is injected at large scales and forwardly cascades to smaller scales. In contrast, this is reversed in the EKHI. The wave energy is injected at the electron inertial length and backwardly transfers to the ion inertial scales. As a result, the magnetic energy spectra become softer with time. The three simulations demonstrate similar power-law indices. The expansion continuously induces out-of-plane stochastic electric fields δE_z from magnetic turbulence due to Faraday's law, $\nabla \times E_z \hat{z} = -\frac{1}{c}\frac{\partial \boldsymbol{B}_{\rm ip}}{\partial t}$. As shown in the bottom panels of Figure 6, the electric turbulence spectra δE_z^2 also demonstrate power laws similar to the magnetic turbulence spectra.

The expansion of the magnetic vortices is caused by the higher pressure inside the vortices due to electron acceleration/heating near the center (see Figure 7). We can see that the pressures inside and outside the vortices increase with time, and the pressure ratio of the inside versus the outside decreases, implying that the accelerated electrons escaped from the vortices and gradually reduced the expansion of the vortices. The electrons inside the vortices are accelerated stochastically by the inductive electric fields and produce energy power-law spectra with a two-stage evolution as demonstrated in Figure 7, corresponding to the two-stage evolution of the magnetic turbulence in Figure 6. All three simulations produce a softer power law during the growth stage (dotted lines) by about $\Omega_i t = 20$. As the domain size increases, the power-law energy spectrum becomes harder because there is more magnetic energy stored in larger domain size simulations, which causes the turbulence to become more violent. For simulation L64W32, the growth stage power-law index is 7.5, which decreases to 6.0 for L128W32 and 4.8 for L128W64. The magnetic vortices continue expanding, causing the trapped electrons to be continuously accelerated to a harder energy spectrum. Once the turbulence reaches the quasi-steady stage, the spectral indices stay stable at around 3.5 in all simulations at similar times to Figure 6.

5. The Scaling of the Simulation Results and Their Implications in Solar Flares

Observations of solar flare X-ray spectra can be used to infer the electron energy spectra as described in Section 2.2. The spectra often associated with these observations are power laws

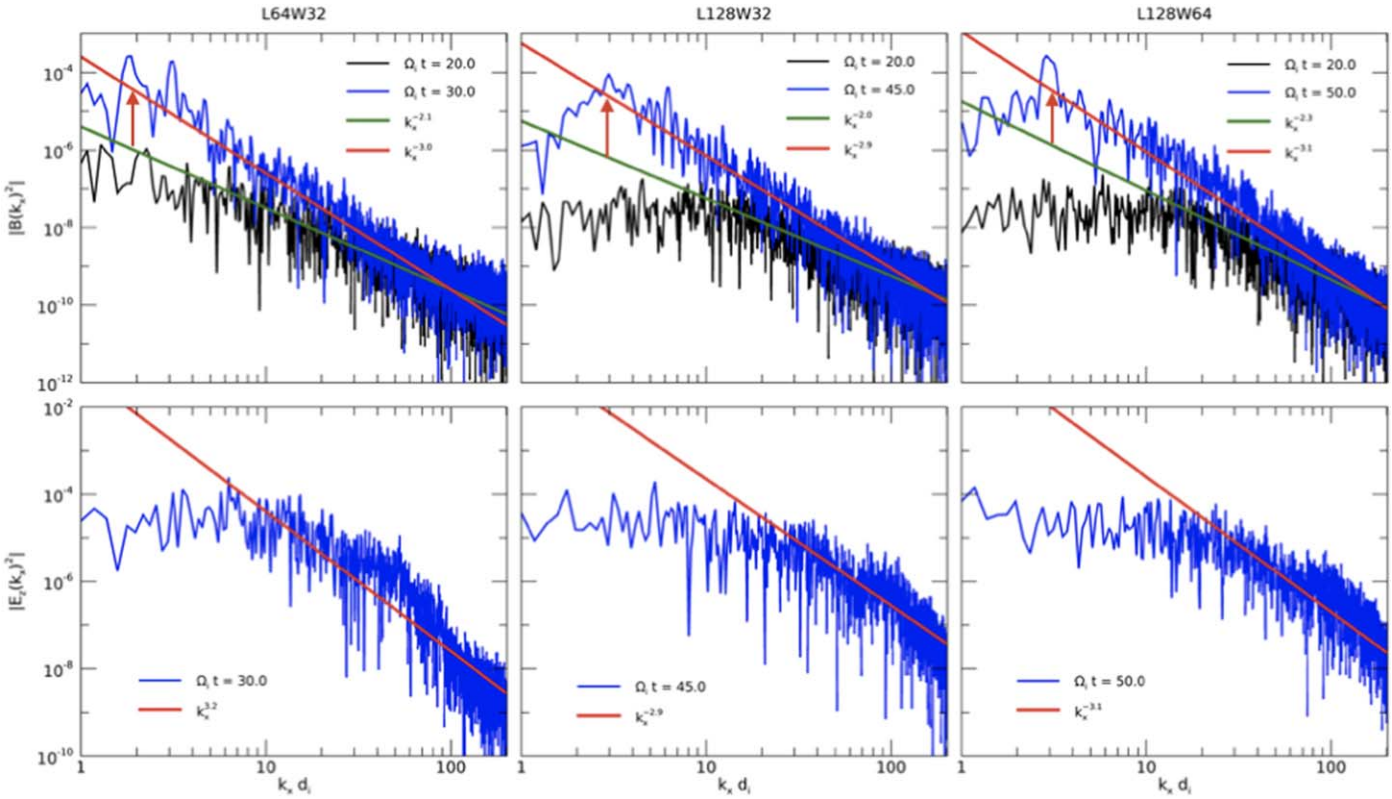

Figure 6. Top: the evolution of the magnetic turbulence power spectra associated with each simulation. The green line represents the power law of the magnetic energy spectrum when it first develops. The red line represents the power law at the quasi-steady stage when the power law stops evolving. Bottom: the electric field turbulence power spectrum of each simulation at the quasi-steady stage.

with a two-stage evolution of the index from a soft index (−6) to a harder index (−3; Benz 2017). Our simulations demonstrate a similar two-stage evolution. However, the domain of PIC simulations is much smaller than solar flare acceleration regions due to the limitations of the capability of currently available supercomputation. For an initial density of $n_{i0} \sim 10^8\,\mathrm{cm}^{-3}$ in the corona, $d_i = c/\omega_{pi} \sim 10^3$ cm, and with a domain size of $128d_i$, we get a scale of $\sim 10^5$ cm for our largest simulation (L128W64), while flaring loops have a scale of about 10^9 cm $\sim 10^6 d_i$. Similarly, the temporal scale of simulation L128W64 is $\Omega_i t = 144$, which is about 10^{-2} s for the asymptotic magnetic field $B_0 \sim 1$ G in the corona, while observations have typical timescales of $\sim$750 s in the solar corona (Benz 2017). This presents the question of how well we can use PIC simulations to quantitatively understand observations of solar flares and, in turn, further improve our future model. In this section, we will first quantitatively define the evolution stages of the EKHI and then showcase how the simulation domain quantitatively affects the two-stage nonlinear evolution of the EKHI. Afterward, we propose a scaling method to extrapolate the PIC simulation results to observational scales and compare the features of simulations to observations in Section 5.4.

5.1. A Quantitative Definition of the Growth and Quasi-steady Stages of the EKHI

As shown previously in Section 4.3, the EKHI evolves in two stages: a growth stage followed by the quasi-steady stage of the EKHI when it is at its peak. Up until now, the evolution of the EKHI has not been well defined quantitatively.

To better describe the nonlinear evolution of the EKHI, we give a quantitative definition for the linear and nonlinear growth stages. From the linear theory, turbulent fields grow exponentially:

$$\delta E_z \propto \delta E_z e^{\gamma t}. \tag{5}$$

Thus, we choose to fit the temporal evolution of the EKHI-induced electric field δE_z to determine the linear and nonlinear stages. As an example, we demonstrate the fitting of the largest simulation, L128W64, in Figure 8. We calculate δE_z using $\langle \delta E_z^2 \rangle^{1/2} = [E_z^2 - \langle E_z \rangle^2]^{1/2}$. We superimpose the growth stage portion of the stochastic electric field evolution with two exponential functions, $e^{\gamma_1 t}$ and $e^{\gamma_2 t}$. We see that the growth rate, $\gamma_1 \sim 0.045\Omega_i$, is of the same order of magnitude as the growth rate from the linear theory $\Omega_e \sim 0.01\Omega_i$, but $\gamma_2 = 0.186 \gg \Omega_e \sim 0.01\Omega_i$. We define the linear growth stage with γ_1, the nonlinear growth stage with γ_2, and the two stages together as the growth stage. As shown in Figure 8, the linear growth stage is short (between $\Omega_i t = 7$ and 10) and transitions into the nonlinear growth stage (between $\Omega_i t = 10$ and 15). After the growth stage, $\langle \delta E_z^2 \rangle$ reaches its peak, leading to a slow growth of the turbulence until it reaches the quasi-steady stage of the turbulence. We can see that the two-stage evolution of the magnetic turbulence and electron energy spectra, shown in Figures 6 and 7, respectively, correspond to the growth and quasi-steady stages of the EKHI. With this new definition, we can also look backward to Figure 3. At the early stage (first column; A_1, B_1, and C_1), the EKHI has already entered the nonlinear growth stage, and in the second and third columns, the EKHI is well into its nonlinear steady stage.

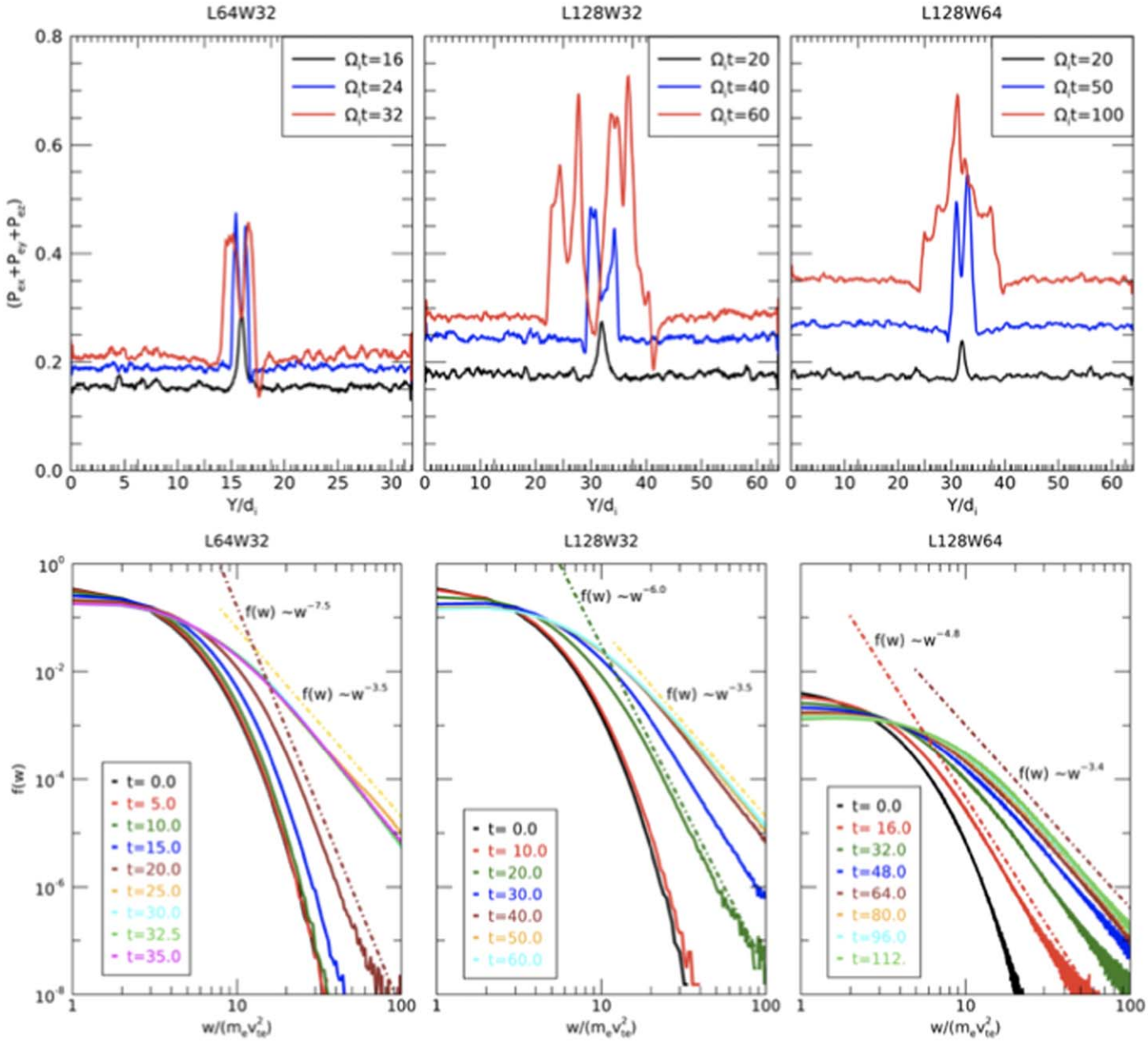

Figure 7. Top: the pressure along a vertical line across a magnetic vortex at different times ($\Omega_i t$) for the same simulations. Bottom: the evolution of the measured electron energy spectra in the magnetic vortices for three MR simulations (L64W32, L128W32, and L128W64). The electron energy power laws shown in each panel (dotted lines) represent the growth stage (the soft spectrum in each plot) and then a hard spectrum during the quasi-steady stage.

5.2. A Quantitative Description of the EKHI Evolution Stages

In this section, we investigate whether the EKHI significantly impacts the MR magnetic energy release process and whether we can relate the evolution stages of the EKHI to the MR process. We show the time evolution of the MR process using the mean in-plane magnetic energy $\langle B_{\rm ip}^2 \rangle$, the electron velocity shear ($|v_{ex}| - |v_{Aex}|$), and the variance of the stochastic electric field ($\langle \delta E_z^2 \rangle = E_z^2 - \langle E_z \rangle^2$) in Figure 9.

Increasing the domain size leads to more magnetic energy stored in the current sheet. As a result, the simulation timescale of the reconnection increases, implying that MR requires more time to release the in-plane magnetic energy $B^2 = B_x^2 + B_y^2$. The MR timescale $t_{\rm MR}$ is approximately determined by $t_{\rm MR} \sim L/v_{\rm A0}$. We see that the start of each MR simulation evolves similarly, with a slow, steady increase at the start until $\Omega_i t \sim 7$, and then MR enters the fast magnetic energy release process. At this stage, the release of magnetic energy peaks, and MR enters its quasi-steady stage. The larger the domain size, the more magnetic energy is required to be released. The total MR energy is approximately proportional to $\bar{B}_{\rm ip}^2 S$, where $S = LW$ is the area of the simulation domain. Doubling the length, L, of the MR simulation (L64W32 to L128W32) or the width, W (L128W32 to L128W64), nearly doubles the MR timescale ($t_{\rm MR}$). Doubling both simultaneously (L64W32 to L128W64) then nearly quadruples $t_{\rm MR}$.

Using the definition of the linear and nonlinear growth stage given in the preceding subsection, we found that the domain size only slightly affects the linear and nonlinear growth stages

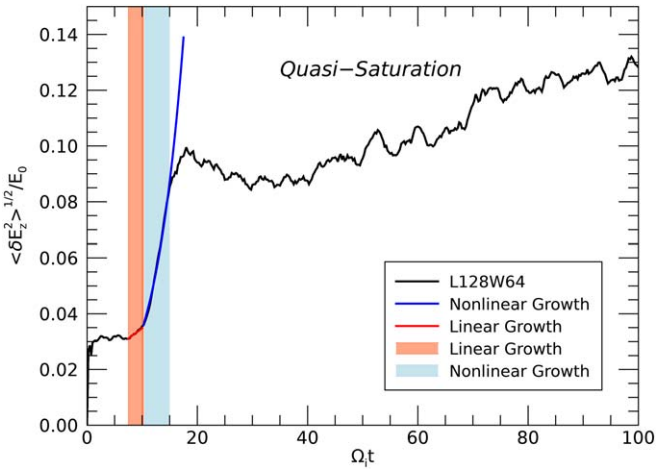

Figure 8. The evolution of the stochastic electric field $\langle \delta E_z^2 \rangle^{1/2} = (E_z^2 - \langle E_z \rangle^2)^{1/2}$ representative of the magnetic turbulence evolution of the EKHI. Two exponential function fits ($\propto e^{\gamma_1 t}$ and $e^{\gamma_2 t}$) are superimposed onto the evolution of the stochastic electric field, where $\gamma_1 \sim 0.05$ is the growth rate of the linear stage of the EKHI, and $\gamma_2 \sim 0.19$ is the growth rate of the nonlinear stage. The red line shows the linear stage of the EKHI ($\Omega_i t = 7$–10), and the blue line shows the nonlinear stage ($\Omega_i t = 10$–20). The shaded areas form the growth stage of the EKHI, which is only weakly affected by the domain size.

of the EKHI shown by the temporal evolution of the inductive stochastic electric field $\langle \delta E_z^2 \rangle$ (see Figure 9(c)). The duration of the growth stage is nearly unaffected because the duration is largely determined by the linear growth rate that is about the electron gyrofrequency Ω_e and uncorrelated with the MR spatial scale. We define the timescale of the growth stage as t_G. After the growth stage, the EKHI enters its long quasi-steady stage, which is equal to $t_{\rm MR} - t_G$. In the larger domain simulations, the evolution of $\langle \delta E_z^2 \rangle$ reaches a more steady state with a slight increase.

The corresponding time evolution of the mean antiparallel velocity shear $\langle |v_{ex}| - |v_{Aex}| \rangle$ near the center of the current sheet is shown in Figure 9(b). We can see that the force-free current sheet has an initial electron velocity shear, $|v_{ex}| - |v_{Aex}| > 0$, which satisfies the threshold of the EKHI. This can explain why, with the proceeding of MR, the EKHI is triggered quickly in all three simulations by $\Omega_i t \sim 7$ (Figure 9(c)). The electron velocity shear continuously accumulates, increasing as the current sheet thins. The EKHI peaks and enters a quasi-steady stage. Then the velocity shear peaks and quickly decreases because of the fast velocity shear dissipation caused by the fast growth of the vortices and broadening of the current sheet. After this, the MR processes enter their quasi-steady stage. The balance between the velocity shear dissipation and the broadening of the current sheet caused by the EKHI and the accumulation of the velocity shear provided by the thinning of the current sheet leads to the saturation of the velocity shear in Figure 9(b). Similar to the evolution of $\langle B_{\rm ip}^2 \rangle$ in Figure 9(a), the larger the simulation domain is, the longer this saturation stage lasts.

Figure 9 tells us that the growth stage of EKHI can also be distinguished in the evolution of the electron velocity shear and the MR magnetic energy release process. The growth stage is between $\Omega_i t \sim 7$ and $\sim$15 and unaffected by the domain size; however, the domain size has a significant influence on the duration of the quasi-steady stage. In Table 2, we use the fraction $t_G/t_{\rm MR}$ to compare the duration of the growth stage of

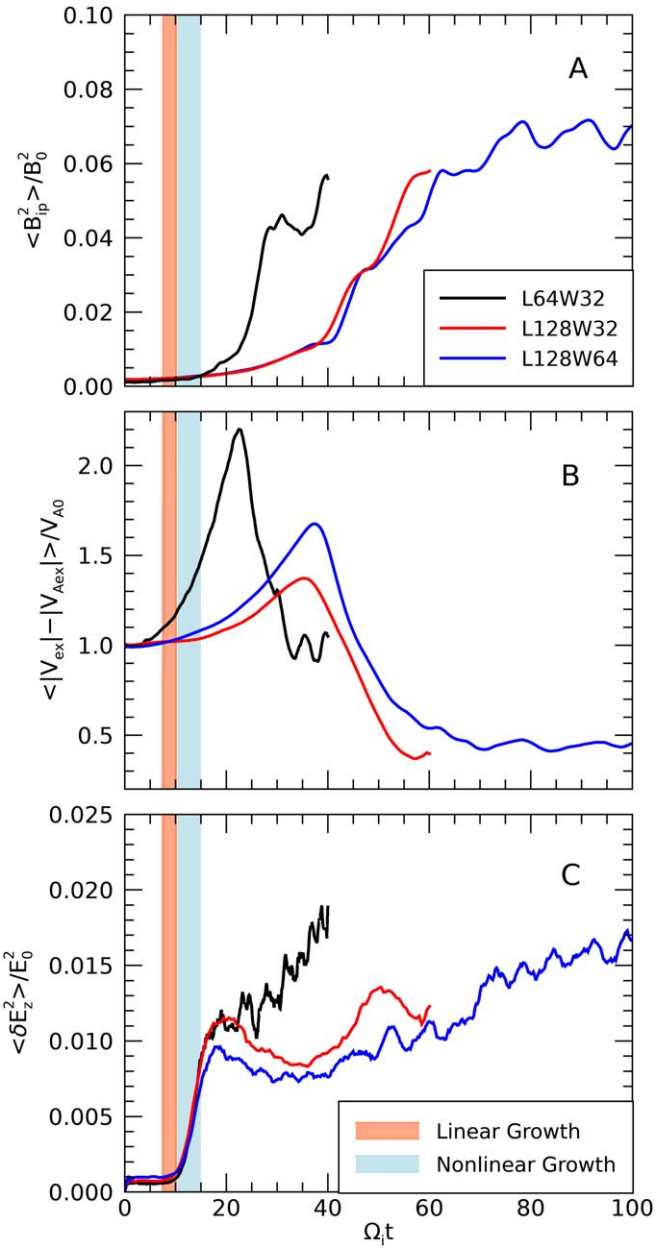

Figure 9. Top panel: the evolution of $\langle B_{\rm ip}^2 \rangle$ with time for three MR simulations with increasing domain size (L64W32, L128W32, and L128W64). $\langle B_{\rm ip}^2 \rangle$, the in-plane magnetic field, was found using the average over a cut through the center of the top left quarter of the simulation domain for B_x and B_y, where $B_{\rm ip}^2 = B_x^2 + B_y^2 \sim B_y^2$, because B_x annihilates and, due to reconnection, generates B_y. Middle panel: the evolution of the velocity shear with time for three MR simulations with increasing domain size (L64W32, L128W32, and L128W64). Using the top left quarter of the simulation domain (where the vortices are located), the velocity shear $(|v_{ex}| - |v_{Aex}|)/v_{\rm A0}$ is calculated using a cut through the center of the current sheet. Bottom panel: the evolution of $\langle \delta E_z^2 \rangle = E_z^2 - \langle E_z \rangle^2$ with time for three MR simulations with increasing domain size (L64W32, L128W32, and L128W64). $\langle \delta E_z^2 \rangle$ was found using the top left quarter of the simulation domain. The red and blue shaded areas refer to the linear and nonlinear growth stages of the EKHI, respectively, which are only weakly affected by the domain size.

the EKHI t_G to the total duration of the MR process $t_{\rm MR}$. We see that in the smallest simulation, the fraction is about $8\Omega_i^{-1}/40\Omega_i^{-1} \sim 0.20$, while in the larger two simulations, this fraction becomes much smaller. For simulation L128W32, the fraction is $8\Omega_i^{-1}/60\Omega_i^{-1} \sim 0.13$, and for the largest simulation

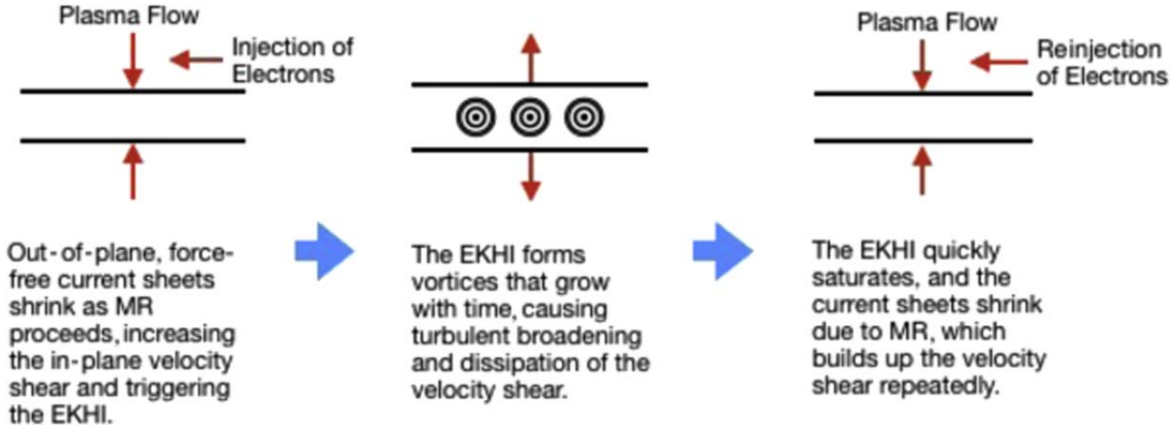

Figure 10. A simple schematic diagram of the shrinking and broadening of the force-free current sheet during turbulent MR.

(L128W64), the fraction becomes $8\Omega_i^{-1}/144\Omega_i^{-1} \sim 0.06$. This suggests that as the simulation domain increases, the timescale of the growth stage of the EKHI becomes more negligible and that the quasi-steady stage dominates the electron acceleration.

5.3. The Continuous Temporal Evolution of the Electron Energy Spectra

In the simulation, we found that the electron acceleration is continuous from the start of the EKHI to the end of the MR process. In Figure 10, we show how the MR process maintains the EKHI. As illustrated in this figure, during the quasi-steady stage of the EKHI, the turbulence tends to broaden the current sheet, competing with MR, which shrinks the current sheet. When the current sheet shrinks, new electrons are reinjected into the diffusion region and accelerated. This competing process maintains continuous electron acceleration.

In Figure 7, we have shown that the electron acceleration is efficient, and on average, the electron energy spectra are accelerated to an energy power law with an index that evolves from ~ -6 to ~ -3 within a few ion gyroperiods. Instead of outputting large amounts of particle data at high time resolution to allow fitting of the time evolution of the electron energy spectral indices, which is computationally costly and infeasible, we opt to calculate the electron energy spectrum of the EKHI using the equation in Che & Zank (2020) introduced in Section 2.1: $f(W) \propto W^{-\alpha}$, where $\alpha = (1 + 4a^2 D/R)/2$ refers to the index of the electron energy power-law distribution, $a = B_{\rm null}/B_0 = 2.5$, and D and R are the spatial scales of the electric field and magnetic vortices, respectively. This equation is obtained assuming the turbulence reaches a steady stage so that we can use it to trace the time evolution of the electron energy spectra during the quasi-steady stage of the EKHI that dominates the electron acceleration process, as we have shown in Section 5.2.

We calculate the temporal evolution of the electron energy power-law index by measuring the spatial scale of the vortices (R) in movie images of j_{ez} reflective of the in-plane magnetic field $B_{\rm ip}$ structure and the spatial scale of E_z (D) in images of E_z to determine values for the index. These movie images are produced by averaging the quantities over the numerical cells and are output with a much higher cadence than the dump files. The largest duration between each image is $0.5\Omega_i^{-1} \sim 50\Omega_e^{-1}$ (for a mass ratio $m_i/m_e = 100$), while the smallest duration between dump files is 10 times longer, $5\Omega_i^{-1}$. The index of the electron energy power-law distribution is then converted to an index representing the X-ray spectral flux (refer to Section 2.2; $\alpha \sim \lambda + 1$, where α is the electron energy spectrum index, and λ is the X-ray spectral index).

Table 2
The Ratios of the Timescales and Spatial Scales

	L64W32	L128W32	L128W64
D	0.73	0.76	1.70
R	2.85	3.05	6.09
D/R	0.26	0.25	0.28
t_G	8	8	8
$t_{\rm MR}$	40	60	144
$t_G/t_{\rm MR}$	0.2	0.13	0.06

Note. The ratio D/R (the electric field scale/the vortex scale) for each simulation during the quasi-steady stage of the EKHI along with the ratio of the duration of the growth stage (t_G) and the total duration of the MR process ($t_{\rm MR}$).

The time evolution of the X-ray spectral index $\lambda = \alpha - 1$ (converted from the electron energy spectral index) is shown for each simulation in Figure 11(a). It is difficult to distinguish the induced electric field during the early quasi-steady stage of the EKHI because the scale of the electric field is too small to be distinguished. For the two larger simulations, this inability to distinguish the scale of the electric field extends further into the quasi-steady stage, which results in later starting times for the evolution of the index as the domain size increases, although the time difference is small and negligible compared to the whole time spectral evolution.

In Figure 11(a), the starting times are $\sim 20\Omega_i t$ for simulation L64W32 and $\sim 35\Omega_i t$ and $\sim 40\Omega_i t$ for simulations L128W32 and L128W64. The starting points used to calculate the spectral index λ are at the transition phase to the steady stage. We can see that for each simulation, the index sharply decreases from ~ 6 to ~ 3 early in the quasi-steady stage of the EKHI, and the index is consistent with the spectral evolution shown in Figure 7. The ratio of the spatial scales (D/R) remains similar for each simulation (as seen in Table 2), indicating that a similar acceleration process is reached. While all three simulations have a similar growth time t_G, the two larger simulations have longer MR timescales ($t_{\rm MR}$), which means that the vortices take longer to develop and expand, staggering the acceleration of new electrons to a harder index and delaying the transition from a soft index (~ 6) to a hard index (~ 3). As a result, the time ratio of the growth stage and the total MR

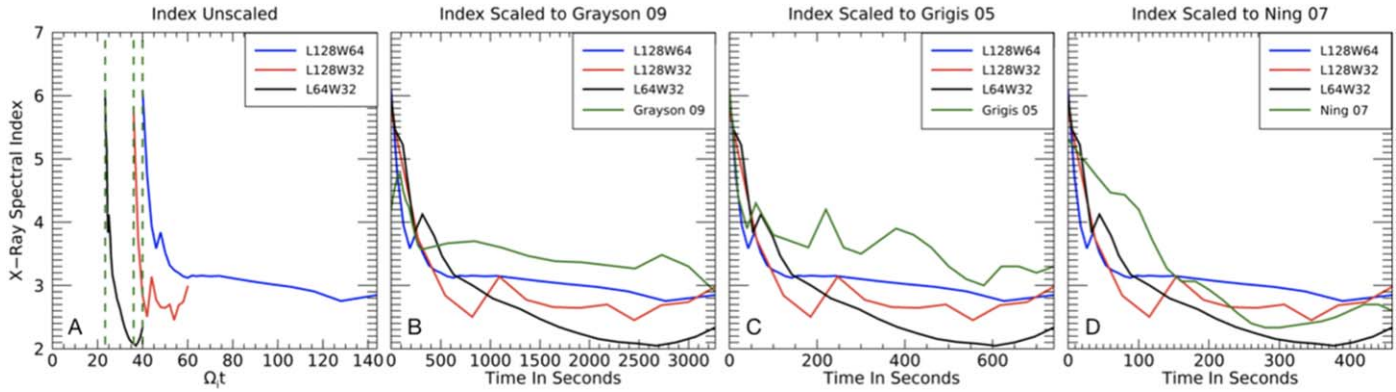

Figure 11. The electron energy spectral index is converted to an X-ray spectral index as it evolves with time. Panel (a) shows the comparison between three simulations of increasing domain size during the quasi-steady stage of the EKHI, while panels (b), (c), and (d) demonstrate a linearly scaled version of panel (a) to observational data, which are, respectively, read out from Figure 1 in Grigis & Benz (2005), Figure 4 in Ning (2007), and the bottom right panel of Figure 1 in Grayson et al. (2009). The temporal scale of each simulation (during the quasi-steady stage) was linearly scaled to match the total time of each observation.

Table 3
Groups of Parameters

Group	B(G)	n_i(cm^{-3})	Ω_i(s^{-1})	ω_{pi}(s^{-1})	d_i(cm)	v_{Ai}(cm s^{-1})
1	1	10^8	9.6×10^3	1.3×10^7	2277	2.2×10^7
2	100	10^{11}	9.6×10^5	4.2×10^8	72	6.9×10^7

Note. Groups of parameters that are used for scaling the time and size of the simulation to observational scales (in cgs units).

Table 4
The Scaled Domain from Simulation to Observation

Group	Timescale (s)	L64W32 (cm)	L128W32 (cm)	L128W64 (cm)
1	460	6.1×10^8	4.2×10^8	9.7×10^7
2	460	1.9×10^9	1.3×10^9	3.1×10^8
1	750	9.8×10^8	6.8×10^8	1.6×10^8
2	750	3.1×10^9	2.2×10^9	5.0×10^8
1	3270	4.3×10^9	2.9×10^9	6.9×10^8
2	3270	1.4×10^{10}	9.4×10^9	2.2×10^9

Note. The linearly scaled domain size of each simulation in centimeters using the timescales of the three different observations of solar flares used in this paper.

simulation time t_G/t_{MR} decreases with the increase of domain size (see Table 2).

The small time ratio t_G/t_{MR} in Figure 11(a) implies a similar, abrupt, two-stage spectral evolution, although in the smallest domain size simulation (L64W32), the steady stage looks insufficient to provide the evolution information.

5.4. The Scaling of the Simulation Results and the Comparison with Observations of Solar Flares

5.4.1. Comparison of the Solar Electron Energy Spectra

As we have seen in the previous section, domain size plays an important role in the discussion of the implications when we compare these simulations to observations. Due to the limitations of computation, the domain size of the simulations is restricted, and the simulations we have carried out have nearly reached the currently available computational capability. To overcome this problem, we need to find a way to scale our simulation results to observational scales. Fortunately, the increase of the spatial scale of the simulations only leads to the increase of the quasi-steady stage timescale of the EKHI, which is nearly linearly proportional to the Alfvénic time L/v_{A0}. In other words, the quasi-steady stage is much longer than the growth stage of the EKHI and dominates the electron acceleration process, implying that the electron energy spectral evolution during the quasi-steady stage of the EKHI can be linearly scaled with the spatial scale. On the other hand, the linear growth stage (before the quasi-steady stage) is too short to be observed in solar flares currently, about 10^{-4} s for the asymptotic magnetic field $B_0 = 1$ G and shorter for magnetic loops whose magnetic field is larger than 1 G. Therefore, we linearly scale the electron energy power-law index's temporal evolution of each simulation during the quasi-steady stage and compare them to flare observations to test our theory.

We scale the temporal evolution of the electron energy power-law index by using a simple ratio defined as

$$R_{\rm scale} = \frac{t_{\rm ob}}{t_{\rm sim}} \sim \frac{t_{\rm ob} v_{A0}}{L}, \quad (6)$$

where $t_{\rm ob}$ is the observational timescale, and $t_{\rm sim}$ is the timescale of the simulation measured during the quasi-steady stage of the EKHI as shown in Figure 11(a) (represented by the dotted green lines); i.e., $t_{\rm sim}$ starts when the vortices first become resolvable and ends at the end of the simulation timescale. The simulation time is converted to seconds by multiplying it with the asymptotic ion gyroperiod Ω_i^{-1} (the final scaled simulation electron energy spectral index evolution is independent of the value of Ω_i). For convenience, the evolution of the scaled electron energy spectra, which starts during the quasi-steady stage, is shifted to start at 0 s. We then rescale the spectral evolution shown in Figure 11(a) to the observation timescales in Figures 11(b)–(d) corresponding to the three selected solar flares that we discuss below.

We choose three flare events with typical and distinctive durations and spectral evolution properties. The first is an M4.9

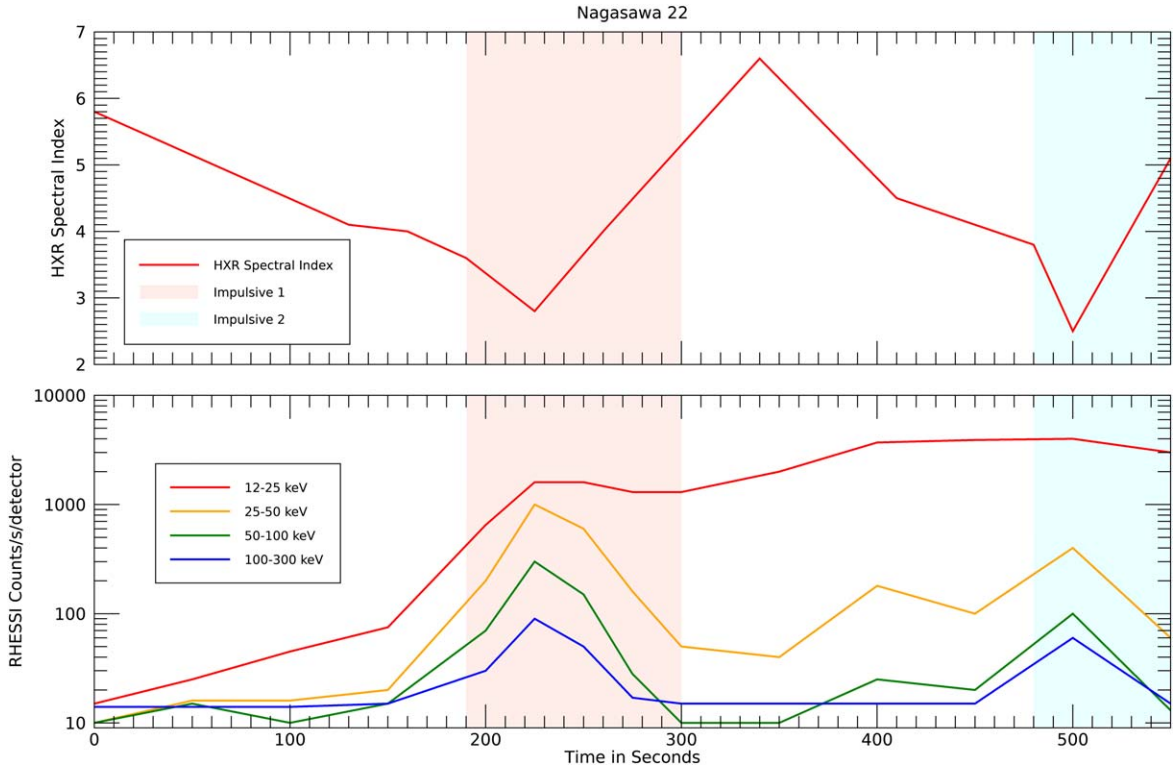

Figure 12. Top: the HXR spectral index evolution of the 2016 July 23 M7.6 solar flare, which clearly demonstrates an SHS evolution of the HXR ($E > 10$ keV) spectral index. Bottom: the RHESSI HXR background-corrected count rate for reference. The two impulsive phases of the flare are highlighted in light red and blue. The observation data is read out from Figures 6(c) and (e) in Nagasawa et al. (2022).

(GOES) solar flare observed by RHESSI on 2002 November 9 from 12:23 to 13:28 UT (Grigis & Benz 2005). Grigis & Benz show the time evolution of the X-ray spectral index of several emission peaks showing an SHS evolution of the index, while the overall trend of the index shows an SHH evolution. The second is an M1.9 flare observed by RHESSI on 2004 September 19 at 17:12 UT (Grayson et al. 2009), which shows the time evolution of the X-ray spectral index with a slow SHH evolution. The third shows an M1.6 flare observed on 2004 November 3 at 03:23:00 UT (Ning 2007) that demonstrates a faster SHH evolution.

In the following, we compare the overall trend of the electron energy spectral evolution (SHH) to our scaled simulation results. The linearly scaled temporal evolution of the power-law indices λ (to observation) are shown in Figures 11(b)–(d). The linear scaling maintains the time ratio $t_G/t_{\rm MR}$; thus, the sharp transition in the electron energy spectra in Figure 11(a) is also scaled to the observational timescale. Interestingly, similar to the X-ray observational electron energy spectral evolution, the scaled simulation spectra also demonstrate an overall soft-to-hard evolution, in particular, the hard spectral transition at an early time in X-ray observations. The consistency between the scaled theoretical results and the observations in Figure 11 will be achieved for the first time by an electron acceleration mechanism. The abrupt transition from a soft to hard index implies that the acceleration process is very efficient, which is consistent with other observations of energetic electron production in solar flares (Vilmer 2012; Benz 2017). Any electron acceleration mechanism with an acceleration timescale comparable to the MR timescale is unable to produce such a sharp electron energy spectral evolution.

We see that each simulation clearly shows a similar SHH trend of the spectral index from ∼6 to ∼3. We notice that the smallest simulation is slightly harder than the other two, while the other two show a more consistent evolution. The duration of the growth stage t_G of the smallest simulation (L64W32) is a large fraction of the total MR simulation time ($T_{\rm MR} \sim 20\%$) as compared to the two larger simulations, whose timescale fractions are ∼10% and ∼5% for simulations L128W32 and L128W64 (see Table 2). This implies that when the duration ratio of the timescales $t_G/t_{\rm MR}$ is small enough ($\lesssim$10% from Figure 11), the simulation results will converge to 1, and we can demonstrate the electron energy spectral evolution with linear scaling. For the kinetic instability of the EKHI in a thin current sheet ($\sim d_i$), the size of the simulation domain is not required to be as large as a solar flare. This is because the domain size only slightly affects the evolution of EKHI in the thin force-free current sheet in MR. Thin current MR guarantees that the current sheet shrinks to d_e and triggers the EKHI at a similar time with the proceeding of MR because $(|v_{ex}| - |v_{Aex}|) > 0$ is currently satisfied at the center of the current sheet where $B_x \sim 0$. During the quasi-steady stage, the electrons are continuously accelerated by EKHI, although the acceleration becomes much slower than in the growth stage. Therefore, our PIC simulations are sufficient to investigate electron acceleration if the domain size is large enough to ensure that $t_G/t_{\rm MR} \lesssim 10\%$.

5.4.2. Comparison of Active Region Spatial Scale

In order to check if our linear scaling is physically reasonable, we investigate the consistency between the

corresponding scaled MR simulation domain size and the active region spatial scale.

The timescale and spatial scales of the simulations have a simple relationship determined with the linear factor $R_{\rm scale}$. We linearly scale the simulation domain size to an observational scale using the same scaling factor as for the timescale:

$$L_{\rm ob} \sim R_{\rm scale} L_{\rm sim}. \quad (7)$$

In the following, we estimate the scale of the acceleration region of the three flares explored in Figure 11 with a linear scaling method similar to what is used for the electron energy spectral index evolution. However, because the MR simulation timescale is nearly proportional to $t_{\rm sim} = L/v_{\rm A0}$, the estimation of the acceleration region size varies with $v_{\rm A0}$, which is determined by the values of the magnetic field and the density of the magnetic loops.

We use two groups of parameters as labeled in Table 3, with group 1 representing the asymptotic parameters in the solar corona and group 2 representing the asymptotic parameters in a flaring region. Using these two groups of parameters, we scale the domain size of each simulation to an observational scale (in cm) in Table 4. In observations, we expect the acceleration region to reach scales of $\sim 10^8$–10^9 cm. If we look at the flaring region parameters (group 2), the spatial scale estimations nearly all fall within the expected range in observation ($\sim 10^8$–10^9 cm), and the asymptotic parameters (group 1) are also all nearly within the range. Our results suggest that linear scaling can reasonably reproduce the solar plasma environment.

As the timescale of the observation increases, so does the estimation of the spatial scale, suggesting that larger acceleration regions produce longer solar flares. We notice that as the simulation domain size increases, the estimation becomes slightly smaller, implying that the smaller domain size may overestimate the size of the acceleration region.

6. Discussion and Conclusions

In this paper, we investigated how MR accelerates electrons to power-law energy spectra in solar flares, a challenging multiscale problem for both numerical and analytical studies. To investigate this problem, we explored a kinetic model recently proposed by CZ in which electrons are accelerated by the EKHI. We connected this kinetic model to a large-scale MHD turbulent MR model, scaled the kinetic results from PIC simulation to observational scales, and then compared them to solar flare observations. We additionally discovered that the linear stage of EKHI is nearly unaffected by the simulation domain size, and the steady saturation stage dominates the electron acceleration process. The two stages of the EKHI are also reflected in the MR magnetic energy release process, which allows the linear scaling of the PIC simulation of EKHI acceleration. We found that the linearly scaled electron energy spectral evolution from the simulations well predicts the sharp X-ray spectral transition observed in X-ray flares.

As discussed earlier, while current sheets of MHD scales can directly thin to d_i, a more likely scenario is that MHD-scale MR triggers KHI and generates vortices. The merging of vortices then triggers kinetic-scale MR. Therefore, we proposed a KHI turbulent MR acceleration model in which small-scale MRs are triggered in thin current sheets ($\sim d_i$), which are generated by large-scale KHI turbulence. Based on the turbulent MR model, our work focused on vortical MR acceleration with a thin current sheet. We used kinetic theory and PIC simulations to define the growth and quasi-steady stages of the EKHI, and then we conducted an analysis of the impact of domain size on the evolution of the EKHI. Through our investigation of the scaling properties, we found that the time duration of the growth stage t_G of the EKHI remains nearly unchanged with increasing domain size. This is because the linear growth rate of the EKHI is about Ω_e, which is independent of the domain size. The timescale of the quasi-steady stage $t_{\rm MR}$ of the EKHI is determined by the magnetic energy release timescale in MR, which linearly scales with the size of the simulation as $L/v_{\rm A0}$.

Thus, we linearly scaled the simulation results using the CZ model. Using the analytical electron energy spectrum of the EKHI obtained by CZ, $f(W) \propto W^{-(1+4a^2D/R)/2}$, we showed a continuous temporal evolution of the electron energy spectral index. Using a linear scaling method drawn from PIC simulations, we scaled the continuous temporal evolution of the electron energy spectral index to observational scales and compared the results to three typical SHH observations of solar flares. We found that the scaled results show a similar SHH two-stage trend of the electron energy spectral index from $\sim$6 to $\sim$3. We then estimated the scale of the acceleration region of the three solar flares and showed that they fall within acceptable observational ranges. This is the first time a theoretical model produced the solar flare SHH electron energy spectral evolution. In particular, the sharp spectral evolution transition from soft to hard index suggests that the electron acceleration mechanism must be efficient, with a timescale that is a small fraction of the solar flare duration. This conclusion is consistent with solar energetic electron observations, referred to as "the big number problem of electrons in solar flares" (Lin 2011; Vilmer 2012; Benz 2017). The consistency between the MR simulation domain size and the solar flare active region spatial scale indicates that the linear scaling is physically reasonable. This consistency suggests that it is unnecessary for the simulation domain to be as large as the solar flare spatial scale. This means that it is sufficient to demonstrate the underlying physics when the size and duration of the simulation are large enough for the saturation stage of MR to be much longer compared to the evolving stages, which are determined by the ratio of the MR timescale and the growth stage timescale $t_{\rm MR}/t_G$. Our study finds that the minimum limit for $t_g/t_{\rm MR}$ is $\sim$10%

Besides the SHH spectral evolution, observation of HXR spectral emission in solar flares can often demonstrate another type of spectral index evolution behavior referred to as SHS. The index of an SHS spectrum evolves from a soft to a hard index and then back to soft, while the SHH spectra start soft and then become increasingly harder. In this paper, we show that our PIC simulations demonstrate the overall trend of SHH spectral evolution. However, we do not discuss or show SHS evolution. In the top panel of Figure 12, we show an example of a solar flare with HXR spectra demonstrating an SHS evolution (Nagasawa et al. 2022). The index evolves from a soft to a hard index during the peak and becomes softer again until another peak occurs, which hardens it further. This is similar to the observation used in Figure 11(c) (Grigis & Benz 2005), in which there are many SHS peaks with an overall trend of SHH. Both figures suggest that the SHS evolution of the spectral index, often seen in observations of solar flares, can still demonstrate an overall trend from a soft index to a harder index or SHH-like behavior.

The reasons for the formation of the SHS spectra are complex. One reason, as suggested by Grigis & Benz (2006), is that the softening of the spectra may be due to the escape of a large number of accelerated electrons from the acceleration region to the footpoints of the loops. This can be inferred from the HXR flux in Figure 12. We can see that the HXR fluxes in higher-energy bands (>25 keV) decrease when the spectrum becomes soft. The bursty MR, for example, caused by MHD KHI instability (Wang et al. 2023), can repeatedly occur in a large solar flare, which causes reinjection and reacceleration of electrons and rehardens the spectrum again. The solar flare we show in Figure 12 has two impulsive phases that are responsible for the hardening of the spectrum. However, these are problems that are still unanswered and are deserving of further exploration from both observation and theory.

In this paper, we have bridged the CZ model to the large-scale turbulent MR models with solar flare observations. While the CZ model demonstrates a large potential in the understanding of solar flare electron acceleration, this model needs to be explored more in the future. For example, a guide field is common in solar flare magnetic field configurations (Qiu et al. 2017; Dahlin et al. 2022), and the CZ model predicts that the electron energy spectral index is proportional to the square of the ratio of the guide field B_g and the asymptotic magnetic field B_0. Additionally, in theory, a weaker guide field produces a stronger electron velocity shear in force-free current sheets (see Equation (1)). Thus, further analysis of how the guide field impacts the development of the EKHI and electron acceleration is under study.

In theory, it is very difficult for us to have a full kinetic treatment of the 3D multiscale problem. Usually, 3D PIC simulations have to sacrifice other physical conditions, such as a much smaller mass ratio or domain size than 2D PIC simulations. One available method is observational studies. In this paper, we evaluate the CZ model with solar flare observations, and we will continue to investigate our model with more solar flare observations. Additionally, the recent in situ MMS observation by Li et al. (2022) and results from Che & Zank (2023) show that in 3D current sheets, the current sheet experiences a filamentary instability that breaks it up into thin current sheets in the third dimension (Che et al. 2011). EKHI is triggered, and the electrons trapped in the magnetic vortices are accelerated to power-law energy spectra. More studies have to be carried out by both theory and observation.

Acknowledgments

C.C. and H.C. acknowledge partial support by NSF CAREER award 2144324 and NASA Heliophysics ECIP funding No. 80NSSC19K1106. C.C. also acknowledges the partial support of NSF EPSCoR RII-Track-1 Cooperative Agreement OIA-2148653. The simulations were supported by the NASA High-End Computing (HEC) Program through the NASA Advanced Supercomputing (NAS) Division at Ames Research Center.

ORCID iDs

C. Crawford https://orcid.org/0000-0001-5834-0807
H. Che https://orcid.org/0000-0002-2240-6728
A. O. Benz https://orcid.org/0000-0001-9777-9177

References

Aschwanden, M. J. 2002, SSRv, 101, 1
Benz, A. O. 2017, LRSP, 14, 2
Borgogno, D., Grasso, D., Achilli, B., Romé, M., & Comisso, L. 2022, ApJ, 929, 62
Brown, J. C. 1971, SoPh, 18, 489
Burch, J. L., Torbert, R. B., Phan, T. D., et al. 2016, Sci, 352, aaf2939
Che, H., Drake, J. F., & Swisdak, M. 2011, Natur, 474, 184
Che, H., & Zank, G. P. 2019, JPhCS, 1332, 012003
Che, H., & Zank, G. P. 2020, ApJ, 889, 11
Che, H., & Zank, G. P. 2023, PhPl, 30, 062110
Che, H., Zank, G. P., Benz, A. O., Tang, B., & Crawford, C. 2021, ApJ, 908, 72
Dahlin, J. T., Antiochos, S. K., Qiu, J., & DeVore, C. R. 2022, ApJ, 932, 94
Daughton, W., Roytershteyn, V., Karimabadi, H., et al. 2011, NatPh, 7, 539
Drake, J. F., Swisdak, M., Che, H., & Shay, M. A. 2006, Natur, 443, 553
Grayson, J. A., Krucker, S., & Lin, R. P. 2009, ApJ, 707, 1588
Grigis, P. C., & Benz, A. O. 2005, ApJL, 625, L143
Grigis, P. C., & Benz, A. O. 2006, A&A, 458, 641
Karimabadi, H., Roytershteyn, V., Wan, M., et al. 2013, PhPl, 20, 012303
Kepa, A., Falewicz, R., Siarkowski, M., & Pietras, M. 2020, A&A, 642, A112
Klein, K.-L., & Dalla, S. 2017, SSRv, 212, 1107
Kliem, B. 1994, ApJS, 90, 719
Kowal, G., Falceta-Gonçalves, D. A., Lazarian, A., & Vishniac, E. T. 2020, ApJ, 892, 50
Kuramitsu, Y., Moritaka, T., Sakawa, Y., et al. 2018, NatCo, 9, 5109
Lazarian, A., & Vishniac, E. T. 1999, ApJ, 517, 700
Li, X., Wang, R., Lu, Q., et al. 2022, NatCo, 13, 3241
Lin, R. P. 2011, SSRv, 159, 421
Medvedev, M. V., & Zakutnyaya, O. V. 2009, ApJ, 696, 2269
Miller, J. A., Cargill, P. J., Emslie, A. G., et al. 1997, JGR, 102, 14631
Nagasawa, S., Kawate, T., Narukage, N., et al. 2022, ApJ, 933, 173
Ning, Z. 2007, ApJL, 659, L69
Nishizuka, N., & Shibata, K. 2013, PhRvL, 110, 051101
Petrosian, V. 2012, SSRv, 173, 535
Pritchett, P. L., & Wu, C. C. 1979, PhFl, 22, 2140
Qiu, J., Longcope, D. W., Cassak, P. A., & Priest, E. R. 2017, ApJ, 838, 17
Raymond, J. C., Krucker, S., Lin, R. P., & Petrosian, V. 2012, SSRv, 173, 197
Torbert, R. B., Burch, J. L., Phan, T. D., et al. 2018, Sci, 362, 1391
Vilmer, N. 2012, RSPTA, 370, 3241
Wang, R., Wang, S., Lu, Q., et al. 2023, NatAs, 7, 18
Zank, G. P., le Roux, J. A., Webb, G. M., Dosch, A., & Khabarova, O. 2014, ApJ, 797, 28
Zeiler, A., Biskamp, D., Drake, J. F., et al. 2002, JGRA, 107, 1230